Research paper

Plasmonic Ag-TiO$_{2-x}$ nanocomposites for the photocatalytic removal of NO under visible light with high selectivity: The role of oxygen vacancies

Yanyan Duan [a,b], Mei Zhang [a], Lan Wang [a], Fu Wang [a,*], Liping Yang [a,b], Xiyou Li [a,*], Chuanyi Wang [a,*]

[a] Laboratory of Environmental Science and Technology, The Xinjiang Technical Institute of Physics and Chemistry, Key Laboratory of Functional Materials and Devices for Special Environments, Chinese Academy of Sciences, Urumqi 830011, PR China
[b] University of Chinese Academy of Sciences, Beijing 100049, PR China

ARTICLE INFO

ABSTRACT

Integration of semiconductors with plasmonic noble metal nanoparticles for visible- light driven photo-catalysis has become an interesting research field recently. In this work, Ag-TiO$_{2-x}$ nanocomposites were successfully synthesized via a facile photochemical reduction process followed by post-annealing. The deposition of Ag nanoparticles greatly increases the light absorption and charge separation. Compared with commercial P25, the Ag-TiO$_{2-x}$ nanocomposites are not only superior in visible-light photocatalytic NO removal, but also in inhibiting the production of NO$_2$, whose toxicity is 4–5 times higher than NO. As confirmed by gas chromatography, the photo-oxidation of NO and selective photo-reduction of NO to N$_2$ occur simultaneously during the process of NO removal by Ag-TiO$_{2-x}$. The oxidation of NO was due to the synergic effect between h$^+$ and •O$_2^-$; while the selective photo-reduction was resulted from introduced oxygen vacancies in TiO$_2$. In addition, the light wavelength dependence measurement reveals that the surface plasmon resonance effect of Ag is responsible for the improvement of the visible-light photoactivity. The present study will provide an alternative approach to design highly selective photocatalysts for NO removal under visible-light.

© 2016 Elsevier B.V. All rights reserved.

1. Introduction

As reported by the Ministry of Environmental Protection of the People's Republic of China, the NO$_x$ (a mixture of NO$_2$ and NO) emissions are increasing year by year [1]. The formation of NO$_x$ mainly derives from power generation plants, coal burning, and automobile exhaust emission, in which atmospheric N$_2$ and O$_2$ react as a result of the high temperatures [2]. The emitted NO$_x$ may lead to photochemical smog, acid rain, haze, and so on [3]. Moreover, NO$_x$ is considered as a significant contributor to a series of diseases [4]. Generally, chemical removal of NO$_x$ is mainly achieved through reduction or oxidation by catalysis, while oxidation is less desirable because it produces more toxic NO$_2$ and NO$_3^-$, which also cannot immediately desorb from the surface of catalysts, and consequently cause the deactivation of catalysts. Over the past decades,

numerous conventional approaches like selective catalytic reduction (SCR), three-way catalysis (TWC), wet scrubbing, bio-filtration, and thermal catalytic process have been explored for NO$_x$ removal at high concentrations from emission sources [5]. However, the above mentioned strategies are not economically feasible to treat air pollutants in urban environments, in which the NO$_x$ is at parts per billion (ppb) levels. Therefore, it becomes more and more critical to develop a practical strategy to remove NO$_x$ by selective reduction at very low concentrations.

Due to the advantages in energy-saving, low cost, green and easy-operation, photocatalysis has been regarded as an alternative technology for the removal of low concentration NO$_x$ in environment. Specifically, TiO$_2$-based semiconductor photocatalysts, which have been extensively studied since 1972, are continuously hold great expectation in photocatalytic NO$_x$ removal at room temperature and ambient pressure because of its strong photocatalytic redox potential, superior corrosion resistance, natural abundance, and non-poisonous [6]. However, utilization of TiO$_2$ as a photocatalyst is limited by its wide band gap and fast recombination of photoinduced charge carriers. The band gap of bulk TiO$_2$

is 3.0 eV and 3.2 eV for the rutile phase and the anatase phase, respectively. The intrinsic band gap makes TiO_2 difficult to use visible-light ($400\,nm < \lambda < 750\,nm$), which accounts for a big fraction of the sun's energy (~45%) [7]. Up to now, considerable work has been carried out on the exploration of efficient TiO_2 composites for visible light photocatalytic NO_x removal, such as graphitic carbon nitride-titanium dioxide (g-C_3N_4-TiO_2) [8], TiO_2-Al composite coatings [9], Mn^{4+}-doped TiO_2 [10], Pd/TiO_2 [11], Au/TiO_2 [12] and so on. However, these materials normally often require tedious synthetic methods which are economically unattractive. Moreover, NO_x removal with those TiO_2-based photocatalysts often through photoxidation, which produces a large amount of toxic NO_2 and NO_3^-.

Integration noble metal nanoparticles (NPs) with TiO_2 is an attractive strategy to extend spectral response and enhance the separation of the photogenerated charge carriers [12–14]. The introduced metal particles (Au, Ag, Cu) can significantly improve photocatalysis performance through localized surface plasmon resonance (LSPR) [15,16]. Among these metals, Ag is considered as the best candidate due to its relatively high stability against oxidation in comparison with Cu and its lower cost than Au.

According to previous report [17], which proposed oxygen vacancies (V_O) in TiO_2 could act as catalytic centers and enhance the selective reduction of NO_x to form N_2, we herein provide a novel approach to produce plasmonic Ag-TiO_{2-x} composites to disclose the roles of Ag and V_O in photocatalytic activity enhancement, especially on the reaction pathways of NO removal. The Ag loading amount was optimized at 2.5% (in mole ratio) based on former evaluation of the loading amount effects [18–20]. The as-resulted Ag-TiO_{2-x} exhibits great stability and excellent visible-light-driven photocatalytic activity for NO removal. More interestingly, Ag-TiO_{2-x} nanocomposites could significantly inhibit the production of toxic NO_2 molecules compared with commercial P25. Considering the experimental observations and theoretical analysis, we speculate that the photocatalytic removal of NO on the as-prepared Ag-TiO_{2-x} might proceed via two path ways: the oxidation of NO is due to the synergic effect between h^+ and $\cdot O_2^-$; while the selective photo-reduction of NO to N_2 and O_2 is due to the introduced V_O which might open an new avenue for selective reduction removal of NO_x.

2. Experimental

2.1. Materials

Silver nitrate ($AgNO_3$, 99.8%), potassium dichromate ($K_2Cr_2O_7$, 99.8%), potassium iodide (KI) and Nitric acid (HNO_3) were obtained from TIANJIN HONGYAN CHEMICAL REAGENT FACTORY. *tert*-Butyl alcohol (TBA) was purchased from Alfa Aesar (China) Chemicals Co., Ltd. Poly (methacrylic acid, sodium salt) (PMAA, average Mw = 9500) was purchased from Sigma-Aldrich. P25 (Degussa) was purchased from Beijing Jiaanheng Science & Technology Co., LTD. All these reagents were used as received without any further purification. Ultrapure water (18.25 MΩ×cm) was used throughout the experiments.

2.2. Sample preparation

2.2.1. Synthesis of Ag nanoclusters
The Ag clusters was synthesized following by a previously reported protocol [21]. Typically, 0.1049 g of $AgNO_3$ was added in 12 mL of ultrapure water in a 150 mL beaker, and then this solution was ultrasonicated vigorously for 5 min till a colorless and transparent solution was obtained. After that, 1.5 mL of PMAA solution (0.8 M) was added into the $AgNO_3$ solution under stirring. The pH

value of the above mixture solution was tuned to ca. 4.25 by drop-wise adding HNO_3 (0.1 M) solution. After a 15 min incubation, the solution was subjected to UV irradiation at $\lambda = 365\,nm$ for 8 min. As time increasing, the bright yellow-solution changed to light pink and then red brown. All the experiments were performed at room temperature.

2.2.2. Synthesis of Ag-TiO_{2-x}
In a typical procedure for the preparation of Ag-TiO_{2-x} nanocomposites, 1 g of P25 was dispersed in 90 mL water by sonication 20 min. Then, a designated volume of Ag nanoclusters solution was added into the above solution under vigorous sonication. After stirring for 5 h, the mixture was centrifuged, and washed with water. Finally, the Ag-TiO_{2-x} was obtained after annealing the resulted mixture under an Ar gas flow (100 sccm) at 250 °C for 2 h with heating rate of 5 °C/min.

2.3. Characterization

The crystal structures of the samples were analyzed by X-ray diffraction (XRD; Bruker D8, using Cu Kα radiation operating at 40 kV and 40 mA, scanning from $2\theta = 10°$ to $90°$). The surface chemical states analysis was studied by X-ray photoelectron spectra (XPS, Thermo Scientific Escalab 250), and all the binding energies were calibrated by using the contaminant carbon (C 1s = 284.6 eV) as reference. The morphology photographs of the samples were recorded by transmission electron microscopy (TEM, JEM-2011 TEM, 200 kV). The Brunauer-Emmett-Teller (BET) surface area (S_{BET}) of all the samples was analyzed by N_2 adsorption/desorption isotherms measurements at 77 K (QUADRASORB IQ, Quantachrome Instrument Corp.). All samples were degassed at 120 °C prior to nitrogen adsorption measurements. Ultraviolet-visible diffusion reflectance spectra (UV-vis DRS) of the powders were obtained on a Shimadzu SolidSpec-3700 DUV using $BaSO_4$ as a standard reference. Raman spectra was recorded at room temperature by using a laser Raman spectrometer (LabRAM HR Evolution RAMAN SPECTROMETER, HORIBA Scientific Ltd.) with an Ar^+ laser (20 mW, 532 nm) as the excitation source. The photoluminescence (PL) spectra of the photocatalysts were measured on a Hitachi F-7000 fluorescence spectrophotometer. Fourier transform infrared spectroscopy (FTS165, BIO-RAD) was employed to analyze the NO_3^- generation on the surface of the photocatalysts during the photocatalytic removal of NO. Electron spin resonance spectra (EPR) were recorded on a Bruker Elexsys E500 spectrometer. The amounts of the metals were determined by inductively coupled plasma optical emission spectrometry (ICP-OES, VISTA-PRO CCD) after the sample was dissolved in a mixed solution (HNO_3, HF and H_2O) using hydrothermal treatment at 180 °C for 3 h. The magnetic performance was conducted by a Physical Property Measurement System (PPMS, Quantum Design, Inc.) at 300 K.

The formation of N_2 was analyzed using online gas chromatography (GC, Agilent 7890A) integrated with a quartz reaction vessel with a closed gas circulation and evacuation system. The detailed analysis procedures are as following. First, put a sample into a reactor, then the reactor was sealed and vacuumed. After achieving a high vacuum, NO (diluted with Ar) was added into the reactor. The same procedure was repeated five times to remove the residual air. Following that, the photocatalytic products were collected for about 6 h.

2.4. Photoelectrochemical measurement

The photocurrent responses and electrochemical impedance spectra (EIS) were performed on an electrochemical station (CHI 660 E, Chenhua, China). KCl (0.1 M) aqueous solution was used as the electrolyte. The photoelectrochemical experiments were
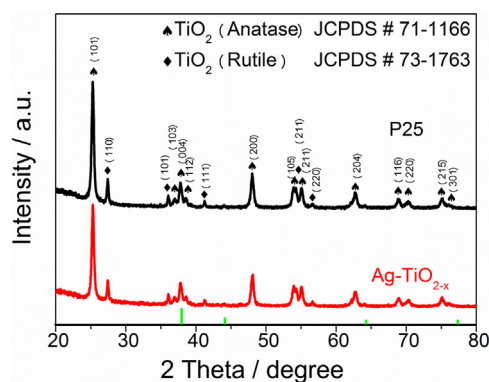
Fig. 1. Powder XRD patterns of P25 and Ag-TiO$_{2-x}$.

carried out in a three-electrode quartz cell. A saturated calomel electrode (SCE) was used as the reference electrode, and a platinum electrode was used as the counter electrode. A bias voltage of −0.20 V was utilized to drive the photo-generated electrons transfer from working electrode to platinum electrode. A 300 W Xe lamp (CEL-HXF300, AuLight, Beijing, China) with a band filter was used as the light source ($\lambda > 420$ nm), which was located 14.5 cm away from the reaction cell.

2.5. Photocatalytic activity measurements

The photocatalytic activity of the samples was evaluated in a continuous-flow setup with volume of 0.785 L ($\pi R^2 H$, $\pi \times 5^2$ cm$^2 \times 10$ cm) at ambient temperature. The concentration of NO was monitored by using a chemiluminescence NO analyzer (Thermo Environmental Instrument Inc. Model 42i) with a measurement range from sub-ppm levels up to 5000 ppm. The NO and NO$_x$ (NO + NO$_2$) concentrations were continuously recorded at every 10 s, and the NO$_2$ concentration was obtained from the concentration difference between NO$_x$ and NO. The light source was provided by a 300 W Xe lamp (420 nm cut off filter) positioned above the chamber. The loading of the photocatalysts used for each experiment was kept at 0.05 g by coating onto a glass dish with a diameter of 5.6 cm. The initial concentration of NO was diluted to ca. 450 ppb by air stream. The Xe lamp was switched on after reaching adsorption-desorption equilibrium. Control experiments demonstrated that no significant NO removal occurred without either light irradiation or photocatalysts. The removal rate of NO was calculated by the following equation: NO removal rate (%) = ($C_0 - C$)/$C_0 \times 100\%$, where C is the NO concentration at a given time, ppb; C_0 refers to the NO concentration at the initial time, ppb.

3. Results and discussion

3.1. XRD characterizations and surface chemical states

Fig. 1 shows the XRD patterns of synthesized samples. The Ag-TiO$_{2-x}$ exhibits similar diffraction patterns with P25. No diffraction peaks belonging to Ag (JCPDS no. 87-0717; the green bars) appear in the patterns which might be due to the fact that the loading amounts of Ag in the present system is beyond the detection limit of the diffractometer, or very limited amount of Ag particles dispersed uniformly on the surface of P25 [22].

XPS measurement was carried out to probe the composition and surface chemical states of the Ag-TiO$_{2-x}$. The XPS method is only sensitive up to ca. 5 nm below the top surface layer [23]. Fig. 2 presents the survey spectrum and high-resolution spectra of Ag 3d, Ti 2p, O 1s orbitals. It is obvious that Ag-TiO$_{2-x}$ contains not only Ti, O, and C, but also a small amount of Ag element (binding energy

at 368 eV), whereas the peak for C 1s is ascribed to adventitious carbon during XPS measurement or the residual PMAA during the sample preparation. From the high-resolution XPS spectrum of Ag 3d in the Ag-TiO$_{2-x}$, the binding energy (BE) corresponding to the Ag 3d$_{5/2}$ peak appears at 367.6 eV, indicating that the formation of metallic Ag [24]. In addition, the BE of Ag 3d$_{3/2}$ is 373.6 eV (Fig. 2b). The difference between BE of Ag 3d$_{5/2}$ and 3d$_{3/2}$ peaks is 6.0 eV, which is also the characteristic of metallic Ag 3d states [25]. It is worth pointing out that the BE of Ag 3d$_{3/2}$ displays a negative shift (ca. 0.7 eV) compared with the standard BE of the bulk Ag [26]. In addition, the spectra of Ti 2p XPS is almost identical for both pristine TiO$_2$ and TiO$_{2-x}$ (Fig. S2). After Ag loading, however, the BE of Ti 2p$_{3/2}$ presents a small positive shift (ca. 0.2 eV) (Fig. 2c), which is due to the strong interaction between Ag and TiO$_{2-x}$ leading to the electron transfer from TiO$_{2-x}$ to Ag. Meanwhile, no shoulder peaks at the BE of 462.5 eV and 456.8 eV for 2p$_{1/2}$ and 2p$_{3/2}$ core level of Ti^{3+} appear, illustrating no Ti^{3+} species on the surface. This is understandable when considering the fact that surface Ti^{3+} tends to be oxidized (e.g., by O$_2$ in air, dissolved oxygen in water, etc.) [27].

Moreover, the asymmetric shape of O 1s peak (Fig. 2d), which can be deconvoluted into three peaks. The peaks centered at 529.6 and 530.25 eV correspond to titanium oxygen bond (Ti−O) [28,29] and hydrogen oxygen bond (O−H) [30], respectively. In addition, the peak at 531.3 eV corresponds to the O-atoms in the vicinity of V$_O$ [31–34]. The molar ratio of O/Ti of Ag-TiO$_{2-x}$ can be derived using the atomic sensitivity factor [35]:

$$n_O/n_{Ti} = (I_O/S_O)/(I_{Ti}/S_{Ti}) \qquad (1)$$

where I and S represents peak area and sensitivity factor, respectively. As a result, n_O/n_{Ti} = 2.35, which is bigger than 2 (stoichiometric ratio of TiO$_2$). The high content of total oxygen might be due to that the surface of TiO$_2$ easily adsorbs some water from the air [36], and hydroxyl groups (corresponding to 530.25 eV in the XPS spectrum) from dissociated water molecules presence thereon [30]. In addition, the content of lattice oxygen (Ti−O) (corresponding to 529.6 eV in the XPS spectrum) in TiO$_2$ is smaller than 2, which is due to the formation of oxygen vacancies during the post-annealing treatment [37].

3.2. Morphological structure

The morphological and structural characteristics of the as-prepared Ag-TiO$_{2-x}$ products were investigated by TEM. Fig. 3 shows the typical TEM and high-resolution TEM (HRTEM) images of Ag-TiO$_{2-x}$ samples. As can be seen from Fig. 3a, some dark spheres (the red pointing arrows) in ~10 nm were dispersed on the top of TiO$_{2-x}$ surface. They were presumed to be metallic Ag due to the high contrast, revealing that Ag NPs were successfully loaded on the TiO$_{2-x}$ surface. Fig. 3b–d present HRTEM images of the Ag-TiO$_{2-x}$ sample, showing that highly crystallized Ag NPs, about 7 nm in size are in close contact with the TiO$_{2-x}$ nanocrystal particles. Note that the interfacial part of the Ag NPs has been reshaped into the layer of TiO$_{2-x}$ partially, indicating that the post-annealing treatment made the formation of close Schottky contact between Ag and TiO$_{2-x}$ [14]. The lattice fringes allow the identification of crystallographic spacing. The average d-spacing values of 0.333 and 0.240 nm correspond to that of the anatase (101) plane and Ag (111) plane, respectively [18,23]. Therefore, Ag NPs were successfully introduced on TiO$_{2-x}$ surface. As reported previously, the close interconnection between Ag NPs and TiO$_{2-x}$ favors the photogenerated electrons transfer [38] and restrains the carriers recombination.
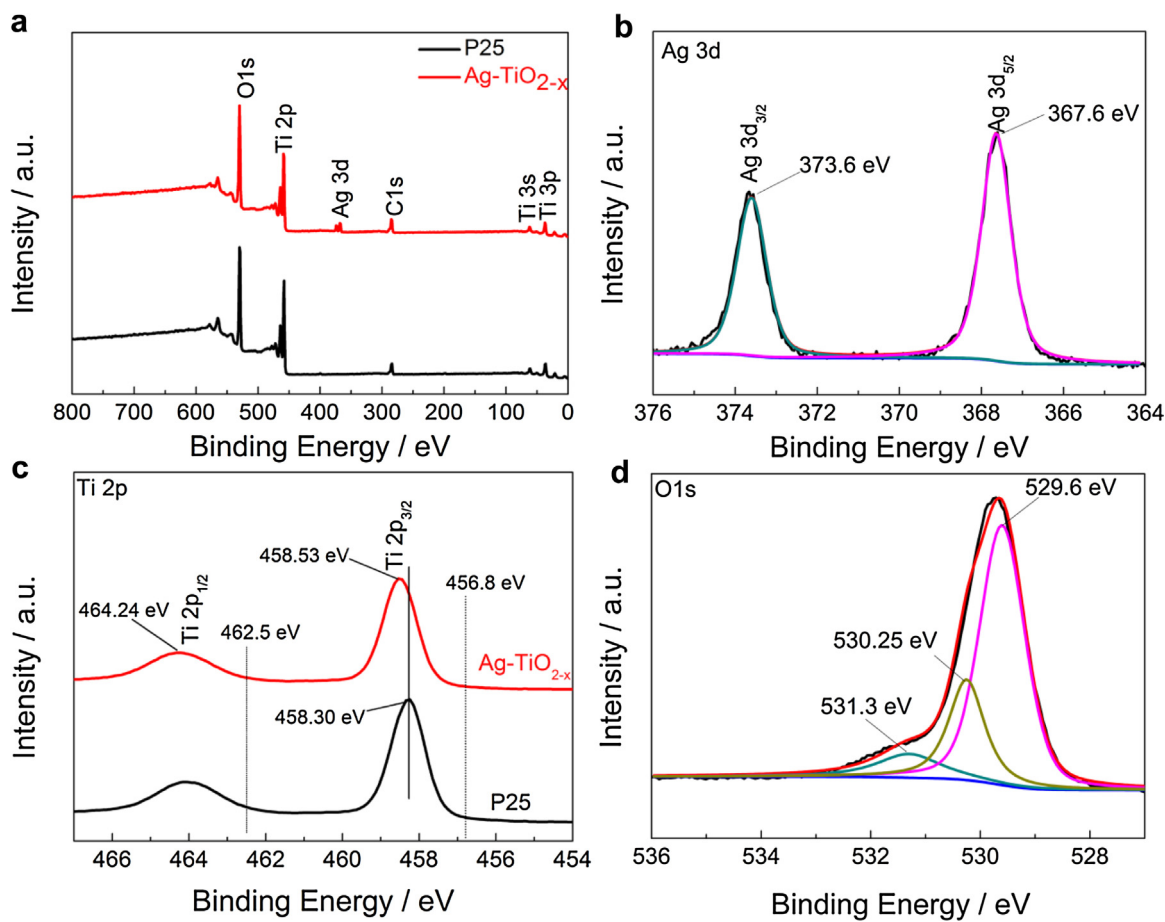
Fig. 2. (a) survey spectrum; (b) Ag 3d; and (c) Ti 2p of P25 and Ag-TiO$_{2-x}$; (d) O 1s of Ag-TiO$_{2-x}$.

3.3. EPR and raman spectra

Species like atoms or molecules with unpaired electrons play an important role in photocatalysis, which can qualitatively and quantitatively measured by EPR. In this work, EPR measurements were conducted under ambient condition and at 100 K to verify the presence of V$_O$. As shown in Fig. 4a, the black line for the commercial P25 shows a negligible signal peak; while the Ag-TiO$_{2-x}$ shows a very strong EPR signal centered on the magnetic field strength of 3365 G, corresponding to the g-factor of around 2.003, which can be attributed to the unpaired electrons trapped on surface oxygen vacancies [39–43]. The EPR results confirm the presence of significant V$_O$ in the samples (Fig. S3) after the post-annealing approach under the oxygen-depleted conditions. Interestingly, at 100 K (Fig. S4), Ag-TiO$_{2-x}$ shows a new broad line which can be attributed to the defect signature of Ti^{3+} [44]. In general, the presence of surface Ti^{3+} tends to adsorb atmospheric O$_2$ and leads to the formation of O$_2^-$, corresponding to an EPR signal at g ≈ 2.02 [29,45,46]. However, no such peak is observed, indicating that Ti^{3+} species only exist in the bulk, which is consistent with the XPS results.

Furthermore, the plots of magnetic field dependence of magnetization also demonstrate the presence of Ti^{3+} spins in Ag-TiO$_{2-x}$. Compared to the commercial P25, Ag-TiO$_{2-x}$ displays stronger magnetization (Fig. S5), which correlates with a higher concentration of unpaired spins from Ti^{3+} [27,29,47]. These results prove that post-annealing treatment of TiO$_2$ (oxygen-depleted condition) leads to oxygen loss and the formation of oxygen vacancies and Ti^{3+} states.

Raman scattering spectroscopic analysis can provide valuable information about phase composition, surface structure and defect (V$_O$) concentrations [25]. Fig. 4b shows the Raman spectra of P25 and Ag-TiO$_{2-x}$, respectively. It should be noted that the residual carbon species on the Ag NPs surface may lead to a strong fluorescence and thereby the Raman peak intensity is very low [48]. Six characteristic peaks (3E$_g$+ 2B$_{1g}$+ A$_{1g}$) of TiO$_2$ anatase phase with frequencies at 142, 197, 398, 516, 519 (superimposed with the 516 cm^{-1} band), and 637 cm^{-1} are observed. The most remarkable feature is that Raman peaks shift toward higher wave number from 141.9 cm^{-1} to 145.6 cm^{-1} for the Ag-TiO$_{2-x}$ compared with P25, further indicating the formation of V$_O$ [11,42,49,50].

3.4. Photocatalytic activity and stability test

The photocatalytic activities of commercial P25 and Ag-TiO$_{2-x}$ nanocomposites were comparatively assessed by the removal of NO under visible irradiation (λ > 420 nm). Fig. 5a illustrates the NO removal rates as a function of irradiation time over different photocatalysts. The dark adsorption differences over diverse photocatalysts were first excluded because they poss specific surface areas [20]. It can be found that commercial P25 showed low but detectable performance for NO removal, which can be attributed to its absorption "tail" extending to ∼410 nm. In contrast, the Ag-TiO$_{2-x}$ composites dramatically improve the photocatalytic efficiency, removing ∼45% of NO under visible light irradiation, which is approximately twice higher than that of the commercial P25. Fig. 5b records the intermediate NO$_2$ generation over different samples. After 15 min of visible-light irradiation, a small amount of NO$_2$ (∼5 ppb) was produced by Ag-TiO$_{2-x}$, lower than that by the commercial P25.
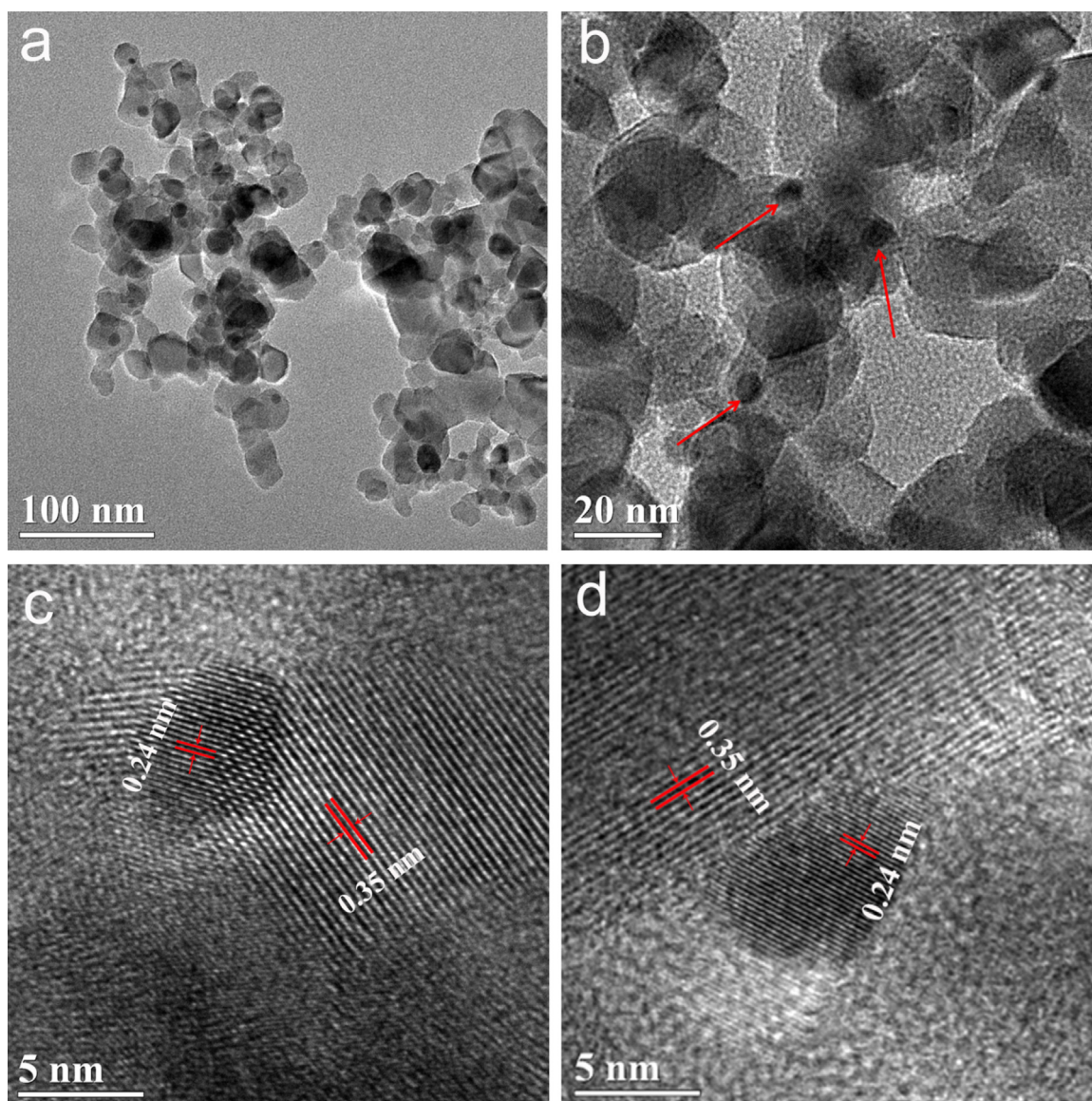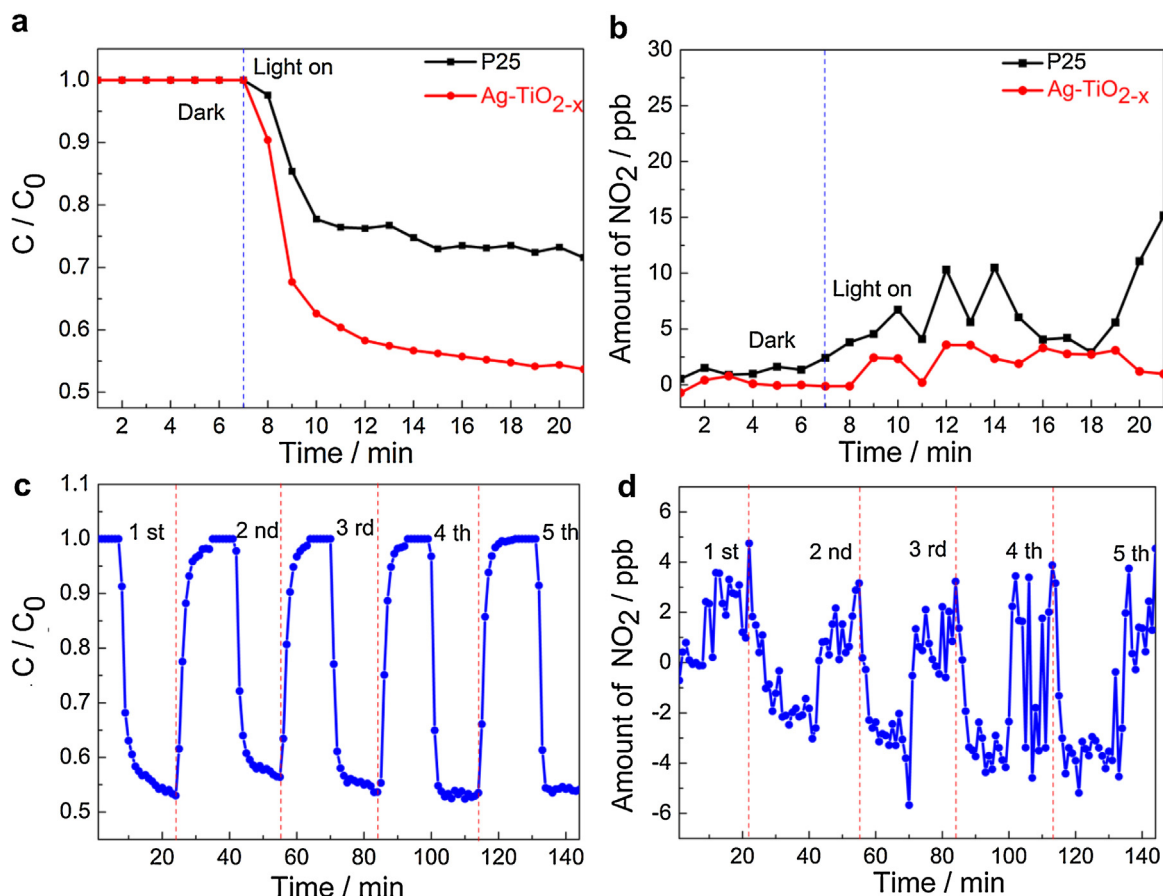
Fig. 3. TEM images of the Ag-TiO$_{2-x}$, obtained by the post-annealed. (a) A low resolution TEM image; (b-d) HRTEM images showing close contact and lattice correlations between Ag NPs and P25 nanocrystals.
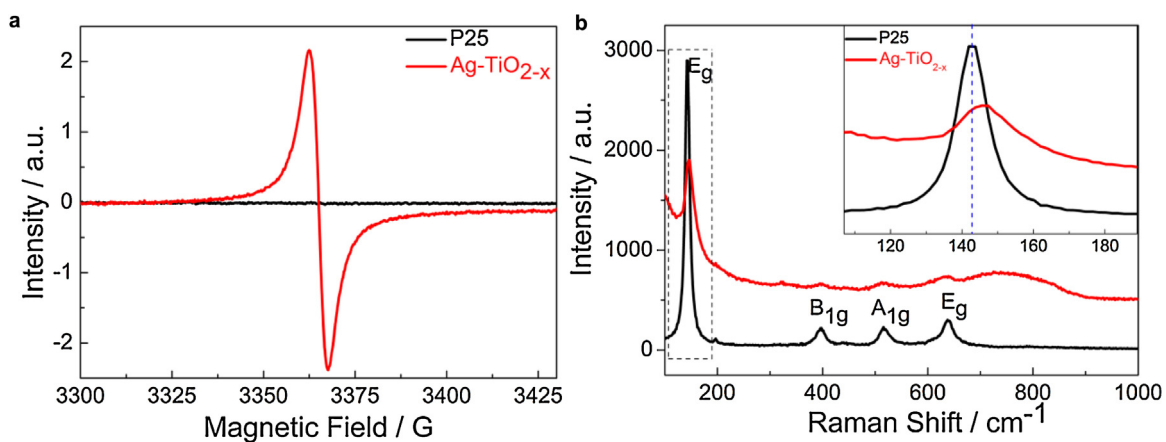
Fig. 4. (a) EPR (measured at room temperature) and (b) Raman spectra of P25 and Ag-TiO$_{2-x}$.

Fig. 5. (a) Comparison of the photocatalytic removal of NO in the presence of P25 and Ag-TiO$_{2-x}$ as a function of irradiation time under visible-light (λ > 420 nm); (b) The NO$_2$ generation over different samples; (c) The stability of Ag-TiO$_{2-x}$ sample in 5 runs of NO removal; (d) The evolution of the NO$_2$ concentration with increasing cycles.

The stability of a catalyst is critical to its application. To test its stability and practicality for NO removal, repeated tests with Ag-TiO$_{2-x}$ were conducted. After five cycles under the same conditions, the photocatalytic activity was largely retained (Fig. 5c), indicating the excellent stability and practicality of the synthesized nanocomposites. Additionally, almost no change in the amount of generated NO$_2$ was observed after each cycle (Fig. 5d), which might be due to the photo-oxidation of NO and selective photo-reduction of NO to N$_2$ occur simultaneously. Comparative tests on TiO$_{2-x}$ (without Ag NPs) and Ag-TiO$_2$ (without Ar annealing treatment) were also performed. TiO$_{2-x}$ exhibits similar property with Ag-TiO$_{2-x}$; in both cases, the amount of the generated NO$_2$ is notably small with barely change after each test cycle (Fig. S6a). However, for Ag-TiO$_2$ (Fig. S6b), the amount of generated NO$_2$ after each cycle increases with increasing recycle number. These results imply that oxygen vacancies truly act as active centers and improve the reaction selectivity to form N$_2$ for NO removal.

3.5. Photocatalytic activity enhancement

To gain an insight into the enhanced photocatalytic activity of Ag-TiO$_{2-x}$ for NO removal, UV–vis DRS were recorded to study the optical properties of P25 and Ag-TiO$_{2-x}$. As shown in Fig. 6a, P25 exhibits majority of light absorption below 400 nm (UV region), but a broad absorption over the entire UV–vis wavelength range was observed (Fig. S7) after it was heat treated at 250 °C in Ar. The Ag-TiO$_{2-x}$ nanocomposites display a stronger absorption between 400 and 600 nm, which could be attributed to the LSPR of spatially confined electrons in Ag NPs [16,51,52]. The LSPR wavelength of metals can be influenced by particle size, particle size distribution, shape,

crystalline structure, the property of the surrounding medium environment and so on [53–55]. The broadening of plasmon peaks may be associated with the wide size distribution of Ag NPs [56,57].

A functioning mechanism of Ag-TiO$_{2-x}$ is tentatively proposed as follows. When Ag NPs and TiO$_2$ are in direct contact, the role of Ag NPs is similar to that of a sensitizer in a dye-sensitized solar cell (Fig. 7) [58]. In the present system, a Schottky barrier forms at the Ag-TiO$_{2-x}$ interface. Under the resonant excitation of the LSPR of the metal particles, a population of energetic electrons will be generated. Then if the "hot electrons" have sufficient energies to overcome the Schottky barrier, they can inject into the conduction band of TiO$_2$, leaving energetic positive charges at Ag NPs which essentially function as holes for the oxidation of NO [15]. This process favors the separation of charge carriers, and thus increases the number of electrons available for the participation in chemical reactions. This is further supported by PL spectral measurements as discussed later.

The band gap values of the synthesized photocatalysts were calculated by plots of $(\alpha h v)^{1/2}$ versus photo energy, as shown in the inset. The band gaps of P25 and Ag-TiO$_{2-x}$ composites are about 3.264 eV and 2.824 eV, respectively. The flatband potential is close to the conduction band position of n-type semiconductor. The conduction band position of P25 and Ag-TiO$_{2-x}$ relative to normal hydrogen electrode (NHE) was calculated to be about −0.407 eV and −0.378 eV from the Mott-Schottky plots (Fig. 6b), respectively. Accordingly, the valence band potentials of P25 and Ag-TiO$_{2-x}$ were calculated to be 2.857 eV and 2.446 eV, respectively. Such electronic state distribution could contribute to the improved photocatalytic efficiency.
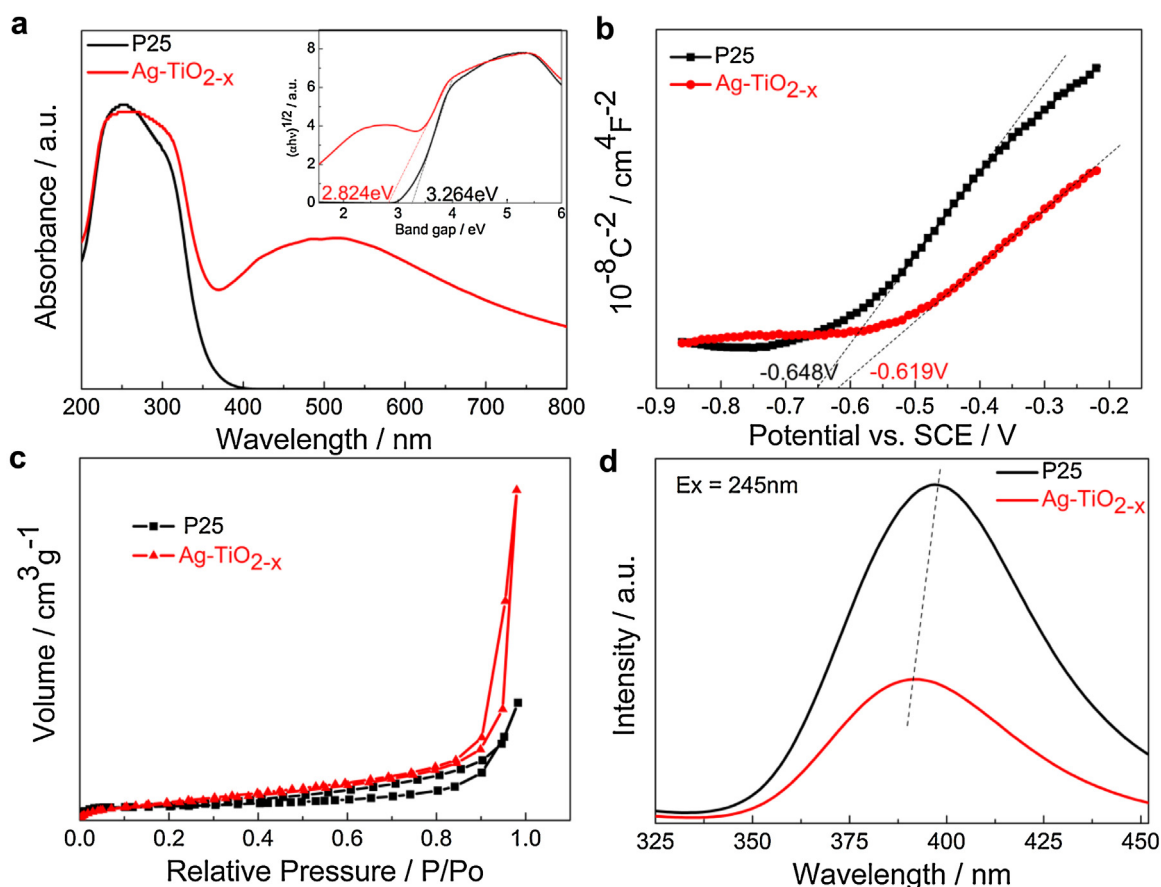
Fig. 6. (a) UV–vis absorption spectra and plots of $(\alpha h)^{1/2}$ versus energy $(h\nu)$ (inset) of P25 and Ag-TiO$_{2-x}$, respectively; (b) Mott-Schottky plot of P25 and Ag-TiO$_{2-x}$ in 0.1 M KCl solution (pH = 7); (c) N$_2$ adsorption-desorption isotherms of P25 and Ag-TiO$_{2-x}$; (d) The PL emission spectra of P25 and Ag-TiO$_{2-x}$ (excited at 245 nm).
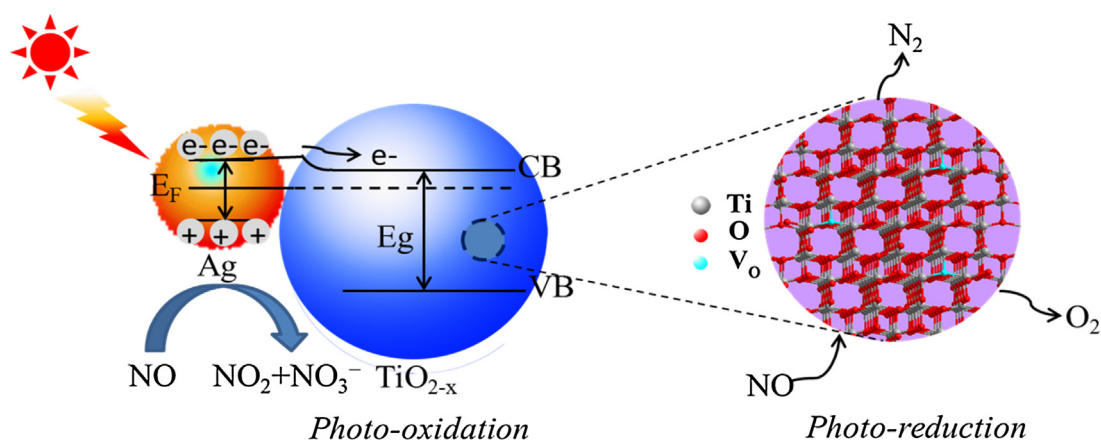
Fig. 7. A plausible mechanism for visible light induced photocatalytic NO removal on Ag-TiO$_{2-x}$.

Specific surface is one of the most important factors primarily influencing the photocatalytic activity. A large surface area can provide more surface active sites for the reaction. The N$_2$ adsorption-desorption isotherms were used to study the surface areas of samples. From Fig. 6c, the S$_{BET}$ of P25 and Ag-TiO$_{2-x}$ is slightly increased from 53.455 m^2 g^{-1} to 62.135 m$^2 \cdot$g^{-1}. However, the activity is greatly difference, indicating that surface area is not the key factor for the improvement of the activity in our system.

PL emission spectra (Fig. 6d) was recorded to probe the separation of photogenerated electrons and holes in P25 and Ag-TiO$_{2-x}$. The PL intensity of Ag-TiO$_{2-x}$ was significantly reduced in comparison with P25 (the absorption of samples is kept approximately

equal at 245 nm), suggesting that Ag NPs modification effectively quench the charge carriers recombination at the interface of P25, then the photocatalytic activity is greatly enhanced. This effect can be further confirmed by the photocurrent measurement. Moreover, the PL emission peak of Ag-TiO$_{2-x}$ exhibits a blue-shifted in comparison with the bulk P25, which could be mainly attributed to the recombination of the photogenerated holes with the single electron oxygen vacancy [31,33,59]. This agrees well with the XPS and EPR analysis results, as discussed above.

The transient photocurrent response of the photocatalysts was examined with several on/off cycles to explore the separation efficiency of photoinduced electron-hole pairs during the photore-
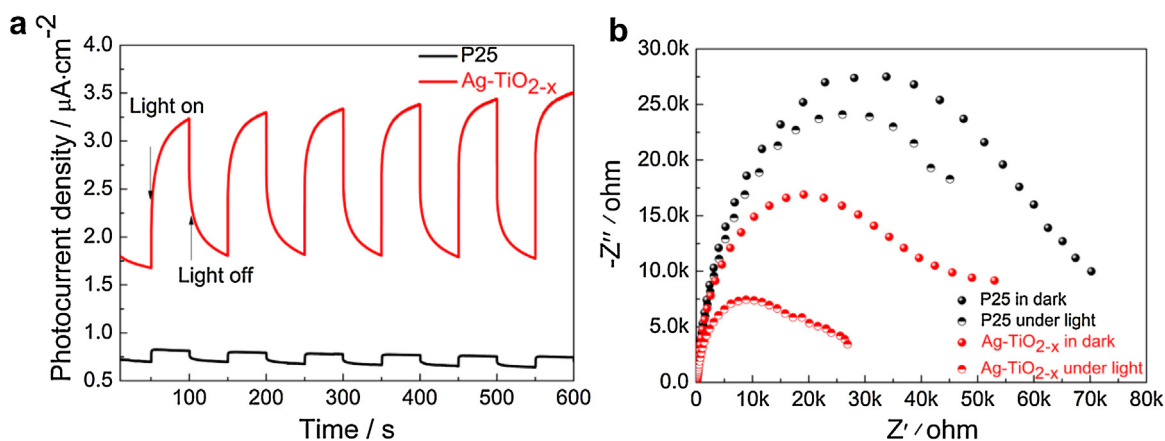
Fig. 8. (a) Transient photocurrent response (TPC) performance of P25 and Ag-TiO$_{2-x}$ under visible-light irradiation; (b) EIS Nyquist plots in dark and under light in 0.1 M KCl aqueous solution.

actions. As can be obviously seen in Fig. 8a, Ag-TiO$_{2-x}$ shows an 8 times higher current density than the commercial P25, which reveals that the mobility of the charge carriers is efficaciously elevated. One important phenomenon is that, after cutting off the light source, the photocurrent of P25 disappears immediately, while Ag-TiO$_{2-x}$ exhibits a residual current. This might be due to the fact that the presence of Ag NPs extends the lifetime of trapped charge carriers reaching the surface of the semiconductor through the improved electron-hole separation at the Ag/TiO$_{2-x}$ interface [60].

EIS measurement is a valid electrochemical approach to investigate the interfacial properties between electrodes and solutions [61,62]. Based on previous studies, a smaller size of semicircle arc of the EIS spectrum means a lower electron-transfer resistance value, implying to a faster interfacial charge transfer [63]. As displayed in Fig. 8b, the Ag-TiO$_{2-x}$ exhibits a smaller semicircular diameter compared to P25 both in dark and under light, illustrating that Ag NPs can effectively improve the electronic conductivity of photocatalysts, which in turn enhances the separation efficiency of photoinduced charge carriers and improves photocatalytic activity under visible-light irradiation.

3.6. Photocatalytic reaction mechanisms

3.6.1. Photo-Oxidation of NO to NO$_2$ and NO$_3^-$

In order to mechanistically understand NO oxidation, analysis of reaction intermediates is crucial. In this work, FTIR measurement was used to qualitatively detect the NO$_3^-$ generation on the surface of the photocatalysts before and after photocatalytic reactions (Fig. 9a). A new absorption band at 1259 cm^{-1} appears after photoreaction, which is attributed to the stretching modes of NO$_3^-$ groups, confirming the generation of NO$_3^-$ during the photocatalytic conversion of NO. Note that the formation of NO$_3^-$ had no negative effect on the cycle activity test of the samples, indicating that NO$_3^-$ did not occupy the photocatalytic reaction active sites. Further experiments were carried out to specify the function of photogenerated electrons and holes as well as other active oxygen species. Herein, potassium iodide (KI), potassium dichromate (K$_2$Cr$_2$O$_7$) and *tert*-butyl alcohol (TBA) were used as photogenerated holes, electrons and •OH scavengers, respectively. The photocatalytic activities of Ag-TiO$_{2-x}$ in different photocatalysis systems under visible-light irradiation are shown in Fig. 9b. The addition of the K$_2$Cr$_2$O$_7$ and KI have a significant negative effect on NO removal, suggesting that photogenerated electrons and holes are all very important in the process of photocatalytic removal of NO. Besides, after adding TBA, the NO removal activity of the sample was slightly changed, indicating that •OH did not contribute to

NO oxidation in this system. From above concled inforamtion, we propose the following mechanisms to describe the processes that may occur, which hypothesis that the oxidation of NO in the present system is due to the synergic effect between h$^+$ and •O$_2^-$.
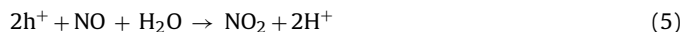
Photogenerated electrons are known to possibly reduce surface-adsorbed oxygen to form superoxide anions [64]:

$$Ag\text{-}TiO_{2-x} + visible\text{-}light \rightarrow h^+ + e^- \tag{2}$$

$$e^- + O_{2ads} \rightarrow {}^\bullet O_2{}^-{}_{ads} \tag{3}$$
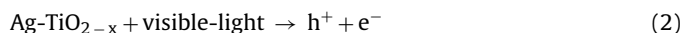
The superoxide anions can directly oxidize NO to a nitrate adsorbate:

$$NO(g) + ({}^\bullet O_2{}^-)_{ads} \rightarrow (NO_3{}^-)_{ads} \tag{4}$$

At the same time, photo-oxidation of NO by h$^+$ leads to the formation of NO$_2$ and NO$_3^-$ [8,65]:

$$2h^+ + NO + H_2O \rightarrow NO_2 + 2H^+ \tag{5}$$

$$NO_2 + h^+ + H_2O \rightarrow NO_3{}^- + 2H^+ \tag{6}$$

3.6.2. Photoreduction of NO to N$_2$ and O$_2$

A less pronounced but persuasive more important observation from Fig. 5d is that, after 5 cycles, the amount of NO$_2$ is still very low. Therefore, we hypothesize that NO was converted into N$_2$ and O$_2$ via reduction.

From the previous work [17], V$_O$ (Fig. 7) can act as catalytic centers and enhance the selectivity of the reaction to form N$_2$. In order to support our assumption that partial NO is photo-reduced, GC measurements were performed to identify constitutes of the reaction products. As shown in Fig. S8a, before illumination, a big peak presences at retention time ca. 3.6 min, which is the signal of mixture gas (NO, O$_2$, and Ar). At the same time, negligible N$_2$ peak also presents due to the presence of trace amount of air. With photoreaction going, the amount of mixture gas decreases because of major reaction consumption of gas. Moreover, as shown in Fig. 10a and b (the amount of residual nitrogen has been subtracted) as well as Table S1, the formation amount of N$_2$ gradually increases until steady-state conditions are reached after ∼ 250 min reaction.

It should be pointed out that the present GC system (Agilent 7890A) is difficult for the detection of NO$_2$. In addition, the amount of O$_2$ (due to the peak overlapping) and the specific amounts of NO and Ar are unknown. Therefore, it is very difficult to quantitatively analyze the ratio of the evolved NO$_2$, N$_2$, and O$_2$ simultaneously. However, the amount of formed N$_2$ is a persuasive proof for the photoreduction as N$_2$ can only result from the reduction of NO to N$_2$ in our closed system. These results clearly support that Ag-TiO$_{2-x}$ changes its photocatalytic selectivity for NO removal from
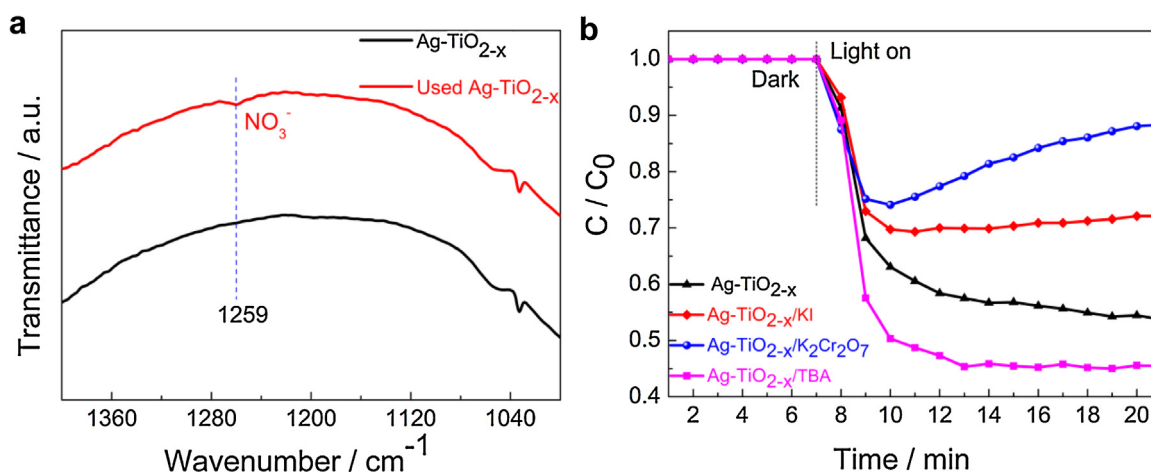
Fig. 9. (a) The FTIR spectra of Ag-TiO$_{2-x}$ before and after reaction, respectively; (b) Comparison of photocatalytic activities of Ag-TiO$_{2-x}$ in different photocatalysis systems under visible-light irradiation.
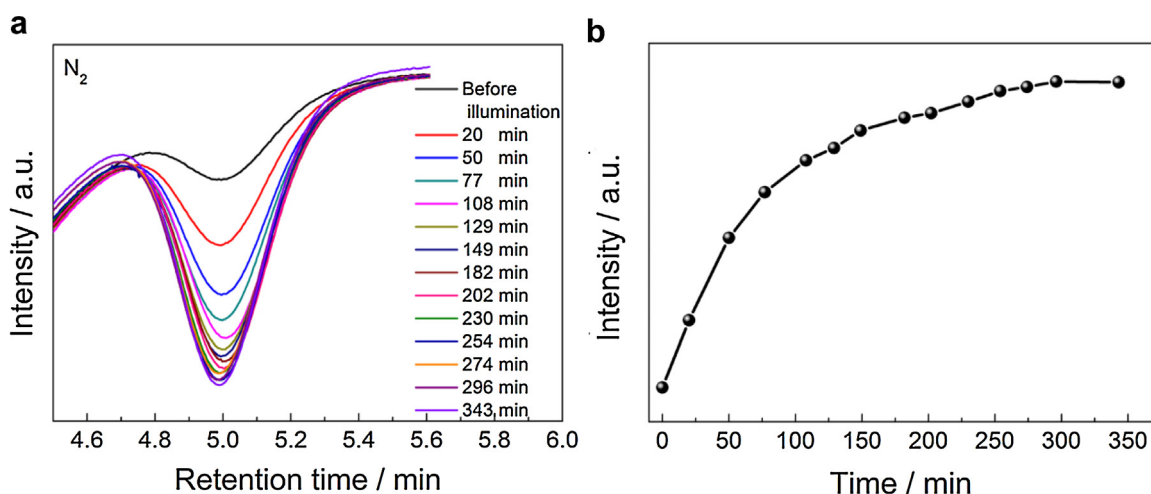
Fig. 10. (a) Typical GC chromatogram of N$_2$ and (b) The formation amount of N$_2$ as a function of time for Ag-TiO$_{2-x}$.

oxidation to reduction. It should be pointed out that the proposed mechanism of photo-reduction is based on primary data, perhaps the same as the previous analysis [17]. Further work is needed to fully understand the mechanism of NO reduction.

3.7. Light wavelength dependence measurement

To elucidate the photoactivity of Ag-TiO$_{2-x}$ as a function of wavelength of incident light, we performed photocatalytic NO removal testing at light wavelength of 365 nm, 420 nm, 520 nm, and 620 nm using LED lamp. The photocatalytic NO removal efficiencies are 40.22%, 44.25%, 39.52%, and 39.83% for 365 nm, 420 nm, 520 nm, and 620 nm, respectively (Fig. 11a). To understand the interplay between the photoactivity and light absorption, differences in light intensities and band-pass should be taken into account because of the spectral variation of incident photons at each wavelength. We normalize the experimental results of NO removal efficiencies using the apparent quantum yield (%, AQY) of NO removal as a function of the incident light wavelength [66,67]:

$$AQY(\lambda) = [number\ of\ reacted\ electrons\ or\ holes]/$$

$$[number\ of\ incident\ photons] \times 100 \quad (7)$$

As a result, the AQY of 365 nm, 420 nm, 520 nm, and 620 nm are 3.58%, 0.581%, 0.726%, and 0.549%, respectively. This is more per-

suasive to show the light wavelength dependence in NO removal efficiency. The result of AQY is shown in Fig. 11b, which reveals several important features. First, the AQY is very dominated by the photoactivity of TiO$_2$ at 365 nm, indicating the highly efficient photoconversion of UV light by TiO$_2$. Second, in the visible region, it is noteworthy that the AQY of Ag-TiO$_{2-x}$ achieves maximum at 520 nm, which is well-matched with the characteristic absorption of the Ag surface plasmon resonance and the broad light absorption. This obtained information is useful for designing photocatalysts with effective light harvesting property and reactivity.

4. Conclusions

In summary, visible-light-driven plasmonic photocatalyst Ag-TiO$_{2-x}$ composites were prepared through a facile photochemical reduction process followed by a simple post-annealing treatment. The prepared Ag-TiO$_{2-x}$ composites exhibit higher visible-light photocatalytic removal of NO relative to TiO$_2$ alone. Our experiments and characterizations indicate that the enhancement in photoactivity can be attributed to the LSPR of Ag NPs, which promotes the visible-light harvesting and reinforces charge separation at Ag-TiO$_{2-x}$ interface. In the present work, the photo-oxidation of NO and selective photo-reduction of NO to N$_2$ occur simultaneously. The oxidation of NO is due to the synergic effect between h$^+$ and •O$_2^-$, while the selective photoreduction of NO to N$_2$ is due
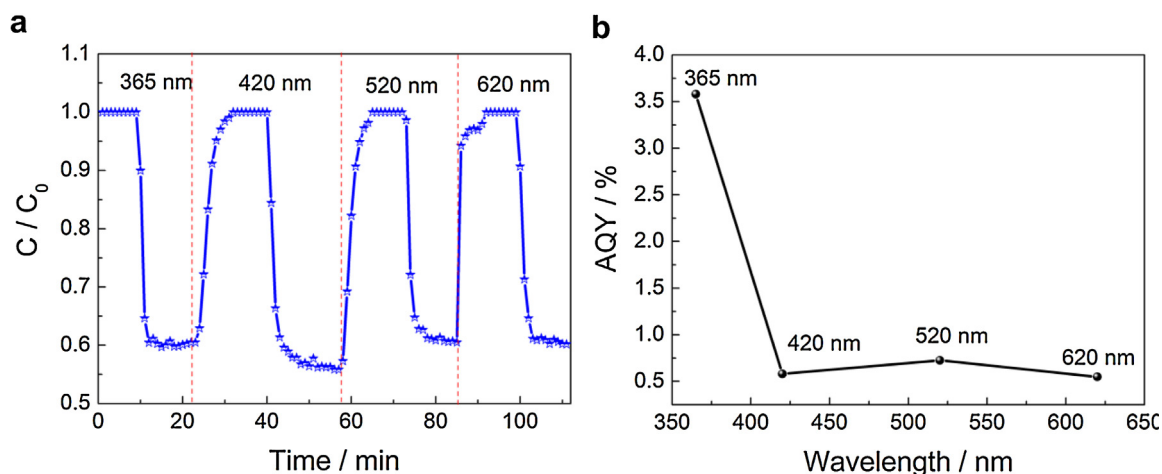
Fig. 11. (a) Photocatalytic NO removal and (b) AQY of Ag-TiO$_{2-x}$ measured at 365 nm, 420 nm, 520 nm, and 620 nm, respectively.

to the formation of V$_O$ during the post-annealing treatment under the oxygen-depleted condition. Moreover, the AQY of Ag-TiO$_{2-x}$ is well-matched with the characteristic absorption of the Ag SPR and the broad light absorption. This work provides a new insight into the different effects of photogenerated reactive species on NO photo-oxidation and V$_O$ on NO photo-reduction, and can open a promising avenue to developing novel materials with effective light harvesting property and reactivity for photocatalytic removal of NO.

Acknowledgments

Appendix A. Supplementary data

Supplementary data associated with this article can be found, in the online version, at http://dx.doi.org/10.1016/j.apcatb.2016.11.023.

References

[1] S. Devahasdin, C. Fan, K. Li, D.H. Chen, J. Photochem. Photobiol. A: Chem. 156 (2003) 161–170.
[2] S. Roy, A. Baiker, Chem. Rev. 109 (2009) 4054–4091.
[3] G. Dong, L. Yang, F. Wang, L. Zang, C. Wang, ACS Catal. 6 (2016) 6511–6519.
[4] C. Su, X. Ran, J. Hu, C. Shao, Environ. Sci. Technol. 47 (2013) 11562–11568.
[5] D.S. Bhatkhande, V.G. Pangarkar, A.A. Beenackers, J. Chem. Technol. Biotechnol. 77 (2002) 102–116.
[6] N. Pinna, M. Niederberger, Angew. Chem. Int. Ed. 47 (2008) 5292–5304.
[7] A.L. Linsebigler, G. Lu, J.T. Yates Jr., Chem. Rev. 95 (1995) 735–758.
[8] J. Ma, C. Wang, H. He, Appl. Catal. B: Environ. 184 (2016) 28–34.
[9] F.L. Toma, G. Bertrand, S.O. Chwa, D. Klein, H. Liao, C. Meunier, C. Coddet, Mater. Sci. Eng. A 417 (2006) 56–62.
[10] M.V. Sofianou, M. Tassi, V. Psycharis, N. Boukos, S. Thanos, T. Vaimakis, J. Yu, C. Trapalis, Appl. Catal. B: Environ. 162 (2015) 27–33.
[11] K. Fujiwara, U. Müller, S.E. Pratsinis, ACS Catal. 6 (2016) 1887–1893.
[12] D. Zhang, M. Wen, S. Zhang, P. Liu, W. Zhu, G. Li, H. Li, Appl. Catal. B: Environ. 147 (2014) 610–616.
[13] Q. Lu, Z. Lu, Y. Lu, L. Lv, Y. Ning, H. Yu, Y. Hou, Y. Yin, Nano Lett. 13 (2013) 5698–5702.
[14] D. Ding, K. Liu, S. He, C. Gao, Y. Yin, Nano Lett. 14 (2014) 6731–6736.
[15] S. Linic, P. Christopher, D.B. Ingram, Nat. Mater. 10 (2011) 911–921.
[16] W. Hou, S.B. Cronin, Adv. Funct. Mater. 23 (2013) 1612–1619.
[17] Q. Wu, R. van de Krol, J. Am. Chem. Soc. 134 (2012) 9369–9375.
[18] J. Yu, J. Xiong, B. Cheng, S. Liu, Appl. Catal. B: Environ. 60 (2005) 211–221.
[19] W. Zhu, P. Liu, S. Xiao, W. Wang, D. Zhang, H. Li, Appl. Catal. B: Environ. 172 (2015) 46–51.
[20] Q. Zhang, Y. Huang, L. Xu, J.J. Cao, W. Ho, S.C. Lee, ACS Appl. Mater. Interfaces 8 (2016) 4165–4174.
[21] L. Shang, S. Dong, Chem. Commun. (2008) 1088–1090.
[22] J. Ma, H. He, F. Liu, Appl. Catal. B: Environ. 179 (2015) 21–28.
[23] X. Xin, T. Xu, J. Yin, L. Wang, C. Wang, Appl. Catal. B: Environ. 176–177 (2015) 354–362.
[24] M. Jin, X. Zhang, S. Nishimoto, Z. Liu, D.A. Tryk, A.V. Emeline, T. Murakami, A. Fujishima, J. Phys. Chem. C 111 (2007) 658–665.
[25] Q. Xiang, J. Yu, B. Cheng, H.C. Ong, Chem. Asian J. 5 (2010) 1466–1474.
[26] Y. Lei, F. Mehmood, S. Lee, J. Greeley, B. Lee, S. Seifert, R.E. Winans, J.W. Elam, R.J. Meyer, P.C. Redfern, D. Teschner, R. Schlogl, M.J. Pellin, L.A. Curtiss, S. Vajda, Science 328 (2010) 224–228.
[27] Z. Wang, C. Yang, T. Lin, H. Yin, P. Chen, D. Wan, F. Xu, F. Huang, J. Lin, X. Xie, Energy Environ. Sci. 6 (2013) 3007–3014.
[28] M. Kuznetsov, J.F. Zhuravlev, V. Gubanov, J. Electron. Spectrosc. Relat. Phenom. 58 (1992) 169–176.
[29] Z. Wang, C. Yang, T. Lin, H. Yin, P. Chen, D. Wan, F. Xu, F. Huang, J. Lin, X. Xie, M. Jiang, Adv. Funct. Mater. 23 (2013) 5444–5450.
[30] Q. Zhang, L. Wang, J. Feng, H. Xu, W. Yan, Phys. Chem. Chem. Phys. 16 (2014) 23431–23439.
[31] F. Lei, Y. Sun, K. Liu, S. Gao, L. Liang, B. Pan, Y. Xie, J. Am. Chem. Soc. 136 (2014) 6826–6829.
[32] K.K. Banger, Y. Yamashita, K. Mori, R.L. Peterson, T. Leedham, J. Rickard, H. Sirringhaus, Nat. Mater. 10 (2011) 45–50.
[33] J. Gan, X. Lu, J. Wu, S. Xie, T. Zhai, M. Yu, Z. Zhang, Y. Mao, S.C. Wang, Y. Shen, Y. Tong, Sci. Rep. 3 (2013) 1021.
[34] L.K. Rao, V. Vinni, Appl. Phys. Lett. 63 (1993) 608–610.
[35] C.D. Wagner, Physical Electronics Division Perkin-Elmer Corp. (1979).
[36] Y. Wang, J. Zhao, T. Wang, Y. Li, X. Li, J. Yin, C. Wang, J. Catal. 337 (2016) 293–302.
[37] S. Li, J. Qiu, M. Ling, F. Peng, B. Wood, S. Zhang, ACS Appl. Mater. Interfaces 5 (2013) 11129–11135.
[38] L. Zhang, J.C. Yu, H.Y. Yip, Q. Li, K.W. Kwong, A.W. Xu, P.K. Wong, Langmuir 19 (2003) 10372–10380.
[39] X. Pan, M.Q. Yang, X. Fu, N. Zhang, Y.J. Xu, Nanoscale 5 (2013) 3601–3614.
[40] J. Zhuang, Q. Tian, H. Zhou, Q. Liu, P. Liu, H. Zhong, J. Mater. Chem. 22 (2012) 7036–7042.
[41] J. Qu, Y. Ge, B. Zu, Y. Li, X. Dou, Small 12 (2016) 1369–1377.
[42] M. Wajid Shah, Y. Zhu, X. Fan, J. Zhao, Y. Li, S. Asim, C. Wang, Sci. Rep. 5 (2015) 15804.
[43] Y. Zhu, Q. Ling, Y. Liu, H. Wang, Y. Zhu, Appl. Catal. B: Environ. 187 (2016) 204–211.
[44] I.R. Macdonald, S. Rhydderch, E. Holt, N. Grant, J.M. Storey, R.F. Howe, Catal. Today 182 (2012) 39–45.
[45] F. Zuo, L. Wang, T. Wu, Z. Zhang, D. Borchardt, P. Feng, J. Am. Chem. Soc. 132 (2010) 11856–11857.
[46] C. Yang, Z. Wang, T. Lin, H. Yin, X. Lü, D. Wan, T. Xu, C. Zheng, J. Lin, F. Huang, J. Am. Chem. Soc. 135 (2013) 17831–17838.
[47] T. Lin, C. Yang, Z. Wang, H. Yin, X. Lü, F. Huang, J. Lin, X. Xie, M. Jiang, Energy Environ. Sci. 7 (2014) 967.
[48] J. Ma, H. Wu, Y. Liu, H. He, J. Phys. Chem. C 118 (2014) 7434–7441.
[49] J. Parker, R. Siegel, Appl. Phys. Lett. 57 (1990) 943–945.
[50] Q. Wu, Q. Zheng, R. van de Krol, J. Phys. Chem. C 116 (2012) 7219–7226.
[51] M. Xiao, R. Jiang, F. Wang, C. Fang, J. Wang, J.C. Yu, J. Mater. Chem. A 1 (2013) 5790.
[52] R. Jiang, B. Li, C. Fang, J. Wang, Adv. Mater. 26 (2014) 5274–5309.
[53] M.A. El-Sayed, Acc. Chem. Res. 34 (2001) 257–264.
[54] H. Chen, L. Shao, Q. Li, J. Wang, Chem. Soc. Rev. 42 (2013) 2679–2724.
[55] L. Vigderman, B.P. Khanal, E.R. Zubarev, Adv. Mater. 24 (2012) 4811–4841.

[56] Z. Bian, T. Tachikawa, P. Zhang, M. Fujitsuka, T. Majima, J. Am. Chem. Soc. 136 (2014) 458–465.
[57] S. Linic, P. Christopher, D.B. Ingram, Nat. Mater. 10 (2011) 911–921.
[58] C. Wen, A. Yin, W.L. Dai, Appl. Catal. B: Environ. 160–161 (2014) 730–741.
[59] G.S. Huang, X.L. Wu, Y.F. Mei, X.F. Shao, G.G. Siu, J. Appl. Phys. 93 (2003) 582.
[60] J. Zhuang, S. Weng, W. Dai, P. Liu, Q. Liu, J. Phys. Chem. C 116 (2012) 25354–25361.
[61] Y.P. Zhu, T.Z. Ren, Z.Y. Yuan, ACS Appl. Mater. Interfaces 7 (2015) 16850–16856.

[62] T. Xu, L. Zhang, H. Cheng, Y. Zhu, Appl. Catal. B: Environ. 101 (2011) 382–387.
[63] Y. Hou, A.B. Laursen, J. Zhang, G. Zhang, Y. Zhu, X. Wang, S. Dahl, I. Chorkendorff, Angew. Chem. Int. Ed. 52 (2013) 3621–3625.
[64] M.R. Hoffmann, S.T. Martin, W. Choi, D.W. Bahnemann, Chem. Rev. 95 (1995) 69–96.
[65] X. Ding, W. Ho, J. Shang, L. Zhang, Appl. Catal. B: Environ. 182 (2016) 316–325.
[66] Z. Jin, X. Zhang, Y. Li, S. Li, G. Lu, Catal. Commun. 8 (2007) 1267–1273.
[67] X. Chen, Y. Li, X. Pan, D. Cortie, X. Huang, Z. Yi, Nat. commun. 7 (2016) 12273.